Article:
Qiao, HY, Nikitas, N orcid.org/0000-0002-6243-052X, Bi, JH et al. (2 more authors) (2019) Mitigation mechanism of longitudinal ribs on rain-wind induced vibrations of stay cables. Fluid Dynamics Research, 51 (4). 045503. ISSN 0169-5983

https://doi.org/10.1088/1873-7005/ab226e

Mitigation mechanism of longitudinal ribs on rain-wind induced vibrations of stay cables

H. Y. Qiao[a], N. Nikitas[c,*], J. H. Bi[a,b,*], J. Guan[a], J. Wang[d,e]

[a] School of Civil Engineering, Tianjin University, Tianjin 300350,China

[b] Key Laboratory of Coast Civil Structure Safety (Tianjin University), Ministry of Education, Tianjin 300350, China

[c] School of Civil Engineering, University of Leeds, Leeds, LS2 9JT, UK

[d] School of Civil Engineering, Tianjin Chengjian University, Tianjin 300384, China

[e] Key Laboratory of Soft Soil Characteristic and Engineering Environment of Tianjin, Tianjin 300384, China

Abstract

For cable stayed bridges rain-wind induced vibrations of stay cables are probably one of the most widespread phenomenon. Aerodynamic countermeasures have been implemented to tackle such vibrations, but there is still not sufficient insight on the inherent mitigation mechanisms. To this goal, a numerical model, based on lubrication theory, was employed in order to study the coupled cable vibration response, aerodynamic forces, and formation and oscillation of rivulets for stay cables equipped with longitudinal ribs. Coupled equations governing the synchronous cable motion and water film evolution were established in order to understand the effects of several key parameters associated with the vibration mitigation performance of the ribs. Such parameters include the cable inclination angle, the wind yaw angle, the number and the height of the ribs. Computed results were successfully validated against experimental data. For the various studied cases, it was apparent that the ribs did not stop the formation of rivulets, but they could affect both their position and oscillation ranges. Through such a control action they could further affect the oscillation range and frequency content of aerodynamic forces, mitigating or not cable vibrations.

Keywords: Rain-wind induced vibrations; Stay cables; Water film; Lubrication theory; Longitudinal ribs; Vortex vibrations

1. Introduction

Stay cables in cable-stayed bridges experience multiple types of vibration in rain and wind conditions due to their low frequency, small structural damping and relatively low mass. There are various vibration categorisations such as rain-wind induced vibrations (RWIVs), dry galloping (DG), vortex-induced vibrations (VIVs) and wake galloping, with RWIVs being probably the most complex of all. RWIVs are associated with excessive response amplitudes, which can further lead to reduction of the cable life, anchorage fatigue (Li et al., 2015), and damage to external dampers (Matsumoto et al., 2003). According to Gimsing and Georgakis (2012) RWIVs make up 95% of all cable vibrations in cable-stayed bridges.

Various countermeasures, such as aerodynamic (Gu and Du, 2005; Kleissl and Georgakis, 2011; Liu, 2016), structural (Caracoglia and Jones, 2007; Ahmand et al., 2015) and mechanical ones (Casciati and Ubertini, 2008; Fournier and Cheng, 2014; Sun, 2017), have been proposed to mitigate these vibrations. Longitudinal ribs are among the aerodynamic countermeasures

*Corresponding author: J. H. Bi
E-mail address: jihongbi@163.com (J.H. Bi)

that have been previously tested and used for cable-stayed bridges for investigating their mitigation efficiency and underlying mechanism. They were first presented by Matsumoto and Shiraishi (1990) specifically against rain-wind induced phenomena; their wind tunnel tests showed that the existence of ribs can directly interrupt the secondary axial flow formed in the near wake and effectively stabilize the cables. Hu et al. (2001) then compared the mitigation effect of spiral and longitudinal ribs in wind tunnel tests, and showed that both types of ribs have a good performance on mitigating RWIVs. Namely, longitudinal ribs can divide the rain water film around the cable into several small rivulets, and disturb the generation of a regular vortex. Furthermore, their height is much lower than spiral ribs with a similar mitigation effect. Li et al. (2005) introduced the equivalent damping ratio, as in aerodynamic damping, to evaluate quantitatively the effects of aerodynamic countermeasures against RWIV instabilities. Through wind tunnel experiments they showed that positive damping contributions are more substantial for the case of longitudinal ribs and helixes than for elliptical rings. Further wind tunnel test by Hung et al. (2016) showed that longitudinal ribs could effectively supress RWIV and DG at the same time in the majority of their experimental cases. Additionally they found that the vibration response was almost identical when checking the effect of rib location by rotating the model around its axis.

Most of the studies above, used wind tunnel tests to investigate the vibration characteristics of cables with longitudinal ribs and the morphology of the associated rivulets. The results revealed that longitudinal ribs have a drastic mitigation effect in most of the studied rainy and windy conditions. However, the mitigation mechanism is still unclear and not thoroughly explained. This is likely to be due to the difficulty in measuring the variation of rivulets in wind tunnel experiments, as rivulets are extremely small, non-canonical, uncontrollable and sensitive to the wind flow. And the existing reference about measuring the rivulets size is about stay cable without aerodynamic measures. Li et el. (2010a) and Li et el. (2010b) used Ultrasonic transmission (UT) technique to measure water rivulet thickness for the first time in the wind tunnel test. Gao et al (2018, 2019) successfully excited and investigated the first, second and third mode RWIVs in wind tunnel tests, and developed an effective computer-vision-based approach to recognize the upper-rivulet dynamics of different modes of RWIVs. Besides, there also appears to be no literature on theoretical models for stay cables with longitudinal ribs experiencing RWIVs. Furthermore, the aerodynamic drag and lift coefficients are inhomogeneous along the cable, and they are difficult to measure accurately because of their time-dependency and sensitivity to perturbations. However, the formation and oscillation of an upper cable rivulet is deemed to be the main factor of RWIVs (Verwiebe and Ruscheweyh, 1998; Peil and Nahrath, 2003; Gu and Du, 2005). On different grounds, the aerodynamic drag force is a decisive parameter in the overall design of a cable-supported bridges, and efforts have been made to generate countermeasures effective in mitigating RWIVs that also keep the drag coefficient at a minimum (Kleissl and Georgakis, 2011; Katsuchi et al., 2017). With all these in mind, it is important to establish a theoretical model and do thorough numerical analysis on the mitigation mechanism of longitudinal ribs encapsulating also their developing aerodynamic forces.

In this paper a theoretical model is outlined which could investigate stay cables with an arbitrary 2D shape. The interaction between the vibration of the cables with longitudinal ribs, variation of water film around them and aerodynamic forces are analysed in detail to study the

mitigation mechanism against RWIVs. To this goal, the effect of several main factors relating to the cable response were parametrically investigated. The numerical results are potentially valuable for further studies on mitigation countermeasures of RWIVs and for paving the way towards similar studies.

2. Theoretical equations

As shown in Fig.1(a) we considered a continuous stay cable with water film of thickness h(θ, t). For this analytical study the water film was assumed to be uniformly distributed along the longitudinal axis of the cylinder. The inclination of the cylinder was denoted by the angle α ($0° \le \alpha \le 90°$), and the yaw angle of the horizontal wind U_0 was determined by the angle β ($0° \le \beta \le 90°$). The angle between the gravity normal g_N and the wind-cable normal velocity U_N vectors is $\delta + \pi/2$, where $\delta = \arctan(\sin\alpha \cdot \tan\beta)$; see Bi et al. (2013). A typical A-A cross-section of the stay cable, taken to be the object of this study, is shown in Fig. 1(b). The distances s*(θ)* between the nominal centre and the surface of the cable were not a constant, with R determining the minimum value of *s(θ)*. Among the limitations there is only one wind speed and just the across-wind cable vibration response that were considered; the density of water and air were kept constant, and the gravity component along the cable and any axial flow effect were not considered.

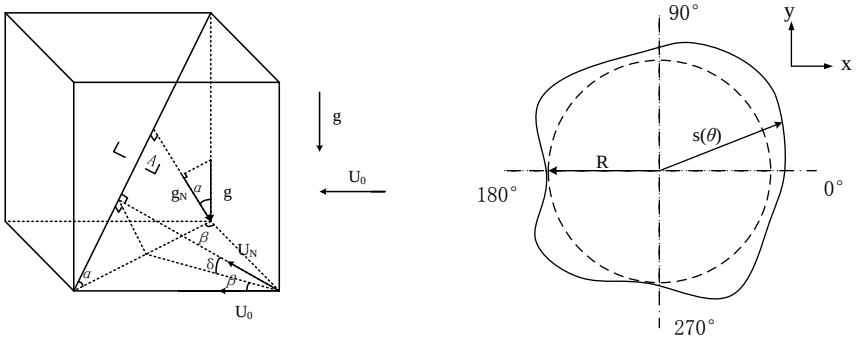

(a) Spatial configuration of stay cable (b) section profile of stay cable with water film

Fig. 1. Model of stay cable.

According to the lubrication theory, the equation of water film around the cable with arbitrary section in non-dimensional form can be written as below.

$$\partial_T H + \left[\frac{\partial_\theta S + \varepsilon\partial_\theta H}{\varepsilon(S+\varepsilon H)} - \frac{1}{\varepsilon}\partial_\theta S - \partial_\theta H\right]\left\{-\frac{3}{2}\left[G\cos(\theta-\delta) - \ddot{Y}\cos\theta + Z\partial_\theta C_P + \frac{C}{\varepsilon}\partial_\theta K\right]H^2 + \frac{3ZC_f N_1^2}{\varepsilon\left[S - \frac{1}{S}(\partial_\theta S)^2\right]}H\right\}$$
$$+\partial_\theta\left\{\left[-G\cos(\theta-\delta) + \ddot{Y}\cos\theta - Z\partial_\theta C_P - \frac{C}{\varepsilon}\partial_\theta K\right]H^3 + \frac{3ZC_f N_1^2}{2\varepsilon\left[S - \frac{1}{S}(\partial_\theta S)^2\right]}H^2\right\} = 0 \quad (1)$$

Dimensionless variables were defined as

$$\mathrm{U}=\frac{\mathrm{R}}{\nu}\mathrm{u_r},\ \mathrm{V}=\frac{\mathrm{R}}{\nu}\mathrm{u}_\theta,\ \mathrm{P}=\frac{\mathrm{h_0^3}}{\rho\nu^2\mathrm{R}}\mathrm{p},\ \mathrm{G}=\frac{\mathrm{h_0^3}}{3\nu^2}\mathrm{g_N},\ddot{\mathrm{Y}}=\frac{\mathrm{h_0^3}}{3\nu^2}\ddot{\mathrm{y}},\ \varepsilon=\frac{\mathrm{h_0}}{\mathrm{R}},\ \xi=\frac{\mathrm{r}-\mathrm{R}}{\mathrm{h_0}},\ \mathrm{Z}=\frac{\rho_\mathrm{g}\mathrm{U_N^2h_0^3}}{6\rho\nu^2\mathrm{R}}$$

$$\mathbf{T}_\mathrm{g}=\frac{\mathrm{h_0^3}}{\rho\nu^2\mathrm{R}}\boldsymbol{\tau}_\mathrm{g},\ \mathrm{C}=\varepsilon^3\frac{\mathrm{h_0}\gamma}{3\rho\nu^2},\ \mathrm{C_p}=\frac{\mathrm{p_g}}{\frac{1}{2}\rho_\mathrm{g}\mathrm{U_N^2}},\ \mathrm{C_f}=\frac{\mathbf{t}_1\cdot\boldsymbol{\sigma}_\mathbf{g}\cdot\mathbf{n}_1}{\frac{1}{2}\rho_\mathrm{g}\mathrm{U_N^2}},\ \mathrm{S}=\frac{\mathrm{s}}{\mathrm{R}},\ \mathrm{K}=\kappa\cdot\mathrm{R},\ \mathrm{T}=\frac{\nu}{\mathrm{Rh_0}}\mathrm{t},\ \mathrm{H}=\frac{\mathrm{h}}{\mathrm{h_0}} \tag{2}$$

The water density ρ, pressure P and dynamic viscosity μ of the water film were as denoted by Lemaitre et al. (2007). The vectors $\mathrm{g_N}$ and $\ddot{\mathbf{y}}$ were also defined as $\mathbf{g_N}=\mathrm{g_N^r}\mathbf{e_r}+\mathrm{g_N^\theta}\mathbf{e_\theta}$ and $\ddot{\mathbf{y}}=\ddot{\mathrm{y}}^\mathrm{r}\mathbf{e_r}+\ddot{\mathrm{y}}^\theta\mathbf{e_\theta}$, where the vector $\ddot{\mathbf{y}}$ is the vector of acceleration of the cable in the across-wind direction. $\boldsymbol{\sigma}_\mathbf{g}$ and $\boldsymbol{\sigma}$ are the stress tensors of air and water respectively. At the interface of water film and air, γ is the coefficient of surface tension and κ is the curvature of the free surface. $\mathrm{h_0}$ is the initial thickness of water film around the cable, and ν is the kinematic viscosity of the water film. For air ρ_g is the air density, $\boldsymbol{\tau}_\mathrm{g}$ is the viscous stress tensor of air, and $\mathrm{p_g}$ is the air pressure at the air-water film interface.

Based on the single-degree-of-freedom assumption, the across wind motion equation of an equivalent stay cable is given by

$$\ddot{\mathrm{y}}+2\omega_0\xi_0\dot{\mathrm{y}}+\omega_0^2\mathrm{y}-\frac{1}{\mathrm{M}}\mathrm{F_y}=0 \tag{3}$$

where ω_0, ξ_0, M, $\mathrm{F_y}$ are the circular frequency, critical damping ratio, mass and lift per unit length of the cable respectively. Note that $\mathrm{F_y}=\int_0^{2\pi}\left[\mathrm{F_r}(\theta)\sin\theta+\mathrm{F}_\theta(\theta)\cos\theta\right]\mathrm{d}\theta$, where $\mathrm{F_r}(\theta)$ and $\mathrm{F}_\theta(\theta)$ are the normal and tangential forces of the water film bottom side $(\mathrm{r}=\mathrm{s}(\theta))$.

The non-dimensional forms of $\mathrm{F_r}(\theta)$ and $\mathrm{F}_\theta(\theta)$, designated as $\chi_\mathrm{r}(\theta)$ and $\chi_\theta(\theta)$ respectively, are given by

$$\chi_\mathrm{r}(\theta)=\frac{\mathrm{h_0^2}}{\rho\nu^2}\mathrm{F_r}(\theta)=\left\{\frac{1}{\mathrm{N_2}}\left(-\frac{\mathrm{R}}{\mathrm{h_0}}\mathrm{P}+\frac{2\mathrm{h_0}}{\mathrm{R}}\partial_\xi\mathrm{U}\right)-\frac{\partial_\theta\mathrm{S}}{\mathrm{N_2S}}\left[\partial_\xi\mathrm{V}+\frac{\mathrm{h_0^2}\partial_\theta\mathrm{U}}{\mathrm{R}(\xi\mathrm{h_0}+\mathrm{R})}-\frac{\nu\mathrm{h_0}}{\xi\mathrm{h_0}+\mathrm{R}}\right]\right\}\Bigg|_{\xi=\mathrm{A}}$$

$$=-\frac{1}{\mathrm{N_2}\varepsilon}\left(\frac{3\mathrm{CK}}{\varepsilon}+3\mathrm{ZC_p}\right)+\left[\frac{2}{\mathrm{N_2}}\partial_\theta\mathrm{S}-\frac{\partial_\theta\mathrm{S}}{\mathrm{N_2S}}+\frac{(\partial_\theta\mathrm{S})^3}{\mathrm{N_2S^2}}\right]\left\{\frac{3\mathrm{ZC_f}\mathrm{N_1^2}}{\varepsilon\left[\mathrm{S}-\frac{1}{\mathrm{S}}(\partial_\theta\mathrm{S})^2\right]}-3\left[\mathrm{G}\cos(\theta-\delta)-\ddot{\mathrm{Y}}\cos\theta+\mathrm{Z}\partial_\theta\mathrm{C_p}\right.\right. \tag{4}$$

$$\left.\left.+\frac{\mathrm{C}}{\varepsilon}\partial_\theta\mathrm{K}\right]\mathrm{H}\right\}$$

$$\chi_\theta(\theta)=\frac{h_0^2}{\rho\nu^2}F_\theta(\theta)=\left\{\frac{1}{N_2}\left[\partial_\xi V+\frac{h_0^2\partial_\theta U}{R(\xi h_0+R)}-\frac{h_0 V}{\xi h_0+R}\right]-\frac{\partial_\theta S}{N_2 S}\left[-\frac{R}{h_0}P+\frac{2h_0\partial_\theta V}{\xi h_0+R}+\frac{2h_0^2 U}{R(\xi h_0+R)}\right]\right\}\Bigg|_{\xi=A}$$

$$=\frac{\partial_\theta S}{N_2 S\varepsilon}\left(\frac{3CK}{\varepsilon}+3ZC_p\right)+\left[\frac{1}{N_2}-\frac{(\partial_\theta S)^2}{N_2 S}+\frac{2(\partial_\theta S)^2}{N_2 S^2}\right]\left\{\frac{3ZC_f N_1^2}{\varepsilon\left[S-\frac{1}{S}(\partial_\theta S)^2\right]}-3\left[G\cos(\theta-\delta)-\ddot{Y}\cos\theta+Z\partial_\theta C_p\right.\right. \quad (5)$$

$$\left.\left.+\frac{C}{\varepsilon}\partial_\theta K\right]H\right\}$$

Eqs. (1) and (3) are the main coupled equations for the water film evolution and the stay cable vibration. The derivation process is shown in detail by Bi et al. (2018).

3. Parameter selection and calculation conditions

For the stay cable with varying surface water film, the coefficients for wind pressure C_p and friction C_f are not constant. The Computational Fluid Dynamics (CFD) software COMSOL Multiphysics is used to compute their instantaneous values and angular distributions. Eqs. (1) and (3) are solved by a finite difference scheme through the numerical software platform of MATLAB. The calculation process uses the same details as previously reported in Bi et al., (2018).

In brief, an equi-spaced distribution of $N=128$ circumferential points and a time-step of $\Delta t=10^{-4}$s were chosen as optimal for the scheme. Following the experimental work of Li et al. (2005), the calculation parameters used in the numerical analysis were: cable radius R of 0.06m, wind velocity of 7.6m/s, cable natural frequency of 1.4375Hz, acceleration of gravity g of 9.8m/s^2, density of water ρ of 10^3kg/m^3, kinematic viscosity of water ν of 10^{-6}m^2/s, surface tension coefficient of water in the air γ of 7.2×10^{-2}N/m, density of air ρ_g of 1.225kg/m^3, and structural damping ratio ξ_0 of 0.217%. At the zero time condition, the water film around the cable was uniform and homogeneous. The initial thickness of water film h_0 is 2.5×10^{-4}m. Fig.2 shows the schematic diagram of a circular section stay cable with two indicative longitudinal ribs. According to the experiment of Li et al. (2010) for the cable with circular 2D shape, the oscillation range for upper rivulets is $\theta\approx30°\sim75°$. Therefore, in Fig. 2 ribs are located at θ_s=30° and θ_s=60° (close to the nominal start and end points). The height and width of ribs are 5mm and 8mm respectively, which is same as the experiment parameters of Li et al. (2007). The function $s(\theta)$ was defined via assigning the relevant uniform 128-point values in MATLAB. The calculation conditions are shown in Table 1. Note that for the indicated one rib setup θ_s=30°; for the three rib setup θ_s=30°, θ_s=45°, θ_s=60°; and for the twelve rib setup θ_s=0°, 30° 60°…360°.

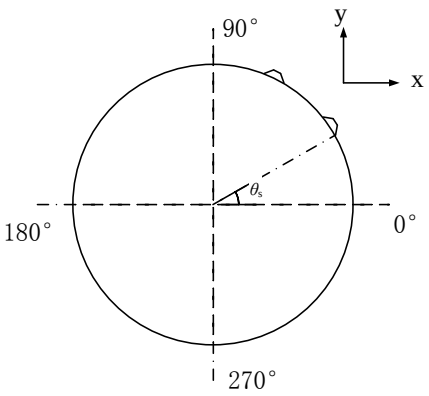

Fig 2. Section profile of studied stay cables with two longitudinal ribs.g

Section	Number of ribs	Cable inclination angle α (°)	Wind yaw angle β (°)	Rib height (mm)
4.1	0(A), 1(B), 2(C), 3(D), 12(E)	30	22	5
4.2	2	15, 20, 25, 30, 35, 40, 45, 50	22	5
4.3	2	30	15, 20, 25, 30, 35, 40, 45, 50, 55	5
4.4	2	30	22	1, 2, 3, 4, 5

Table 1 Parametric variations

4. Numerical results of factors contribute to rain wind induced vibration

4.1 Effect of the rib number

In order to investigate the effect of rib numbers, the cases of a stay cable with zero (A), one (B), two (C), three (D) and twelve (E) ribs are analysed in this part. Likewise the experiment of Li et al. (2007), the height and width of ribs were respectively 5mm and 8mm. Fig. 3 shows the influence of different rib numbers on the relative cable vibration amplitude and the upper rivulet thickness. The term relative for displacements is used to express the ratio between the cable vibration response and its diameter. For the ribbed cable configurations, relative cable vibration amplitudes decrease gradually with the increase of ribs, showing a similar trend to the upper rivulet thickness. It can be seen that when the ribs increase to two, the cable vibration amplitude decreases substantially (amplitude almost half of that in the no-rib case). Thus, a cable with two ribs is considered as the main research focus for the following sections 4.2-4.4. Interestingly, the maximum cable vibration displacement occurs for the case of one rib. For the cable with twelve ribs, the calculation model can be validated against existing experimental findings. Namely, the output cable displacement amplitude is 0.014m (0.12 in non-dimensional form in Fig.3) and falls very close to the experimental value of 0.012m (Li et al., 2007). Also, for the cable without any rib, the displacement 0.048m (0.4 in non-dimensional form in Fig.3) also well replicates the experimental output of 0.049m (Li et al., 2007).

Fig.4 and Fig.5 show the influence of different rib numbers on the mean aerodynamic coefficients and their oscillation ranges respectively. It is clear that the aerodynamic lift variation range should have a closer connection to the cable vibration response. Fig.6 and Fig.7 show the influence of rib numbers on the cable vibration and upper rivulet oscillation frequency and amplitude. Interestingly the dominant frequency of the upper rivulet formation is not close to the structural cable frequency only in the case of a cable with twelve ribs. The existence of twelve ribs impacts the formation and oscillation of the upper rivulet, through a detuning effect, preventing this way excessive cable vibrations and keeping them at a level considerably lower to all other cases. The energy of cable vibration and upper rivulet oscillation change with a similar trend to the cable vibration displacement vs ribs' number.

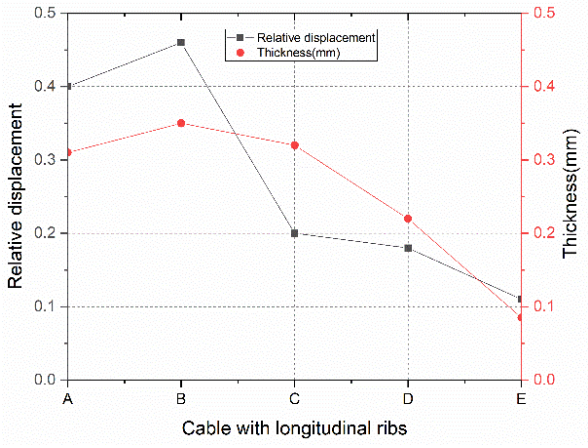

Fig.3 Influence of the ribs' number on cable vibration amplitude and upper rivulet thickness

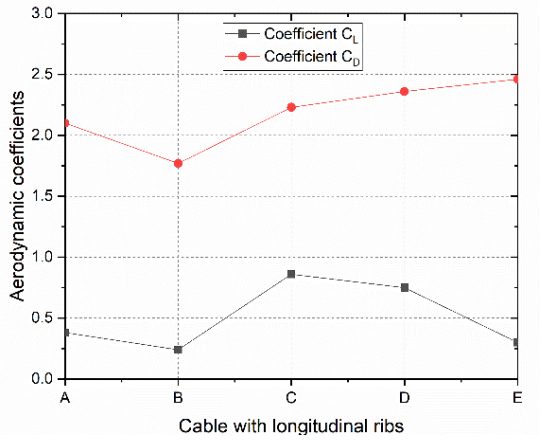

Fig.4 Influence of the ribs' number on aerodynamic coefficients

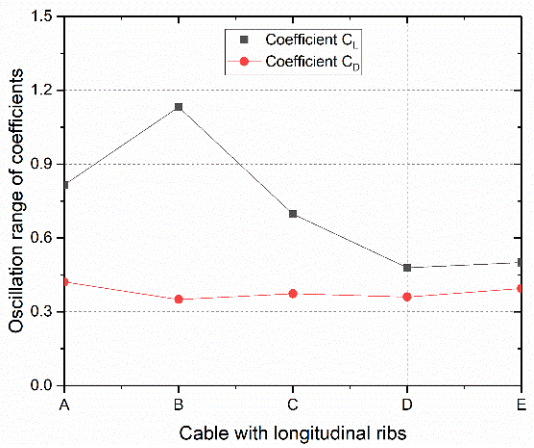

Fig.5 Influence of the ribs' number on aerodynamic coefficients variation range

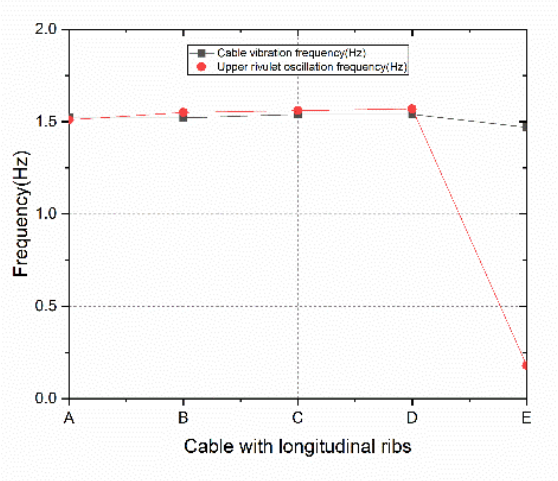

Fig.6 Influence of the ribs' number on cable vibration and upper rivulet oscillation frequency

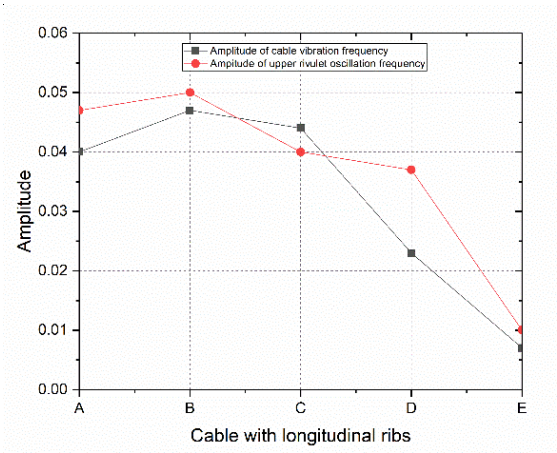

Fig.7 Influence of the ribs' number on cable vibration and upper rivulet oscillation frequency amplitude

Fig.8 presents the calculation of water film evolutions around the stay cable section during $t = 0 - 5s$. For the bare circular cable in Fig.8(a), an upper rivulet exists at the windward direction and oscillates at the cable structural frequency. In Fig.8(b), the existence of two ribs impedes the oscillation of the upper rivulet; the upper rivulet is located around the two ribs and part of the water film slides to the lower rivulet. For the twelve rib scenario in Fig.8(c), the water film gathers around the ribs and the oscillation of upper rivulets is non-apparent.

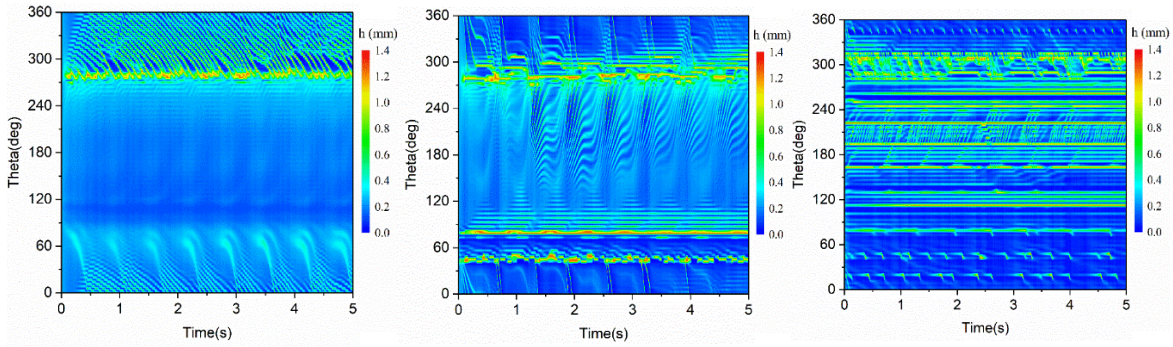

(a) circular cable (b) cable with two ribs (c) cable with twelve ribs

Fig.8 Evaluation of water film around the cable

4.2 Effect of inclination angle

Based on previous wind tunnel tests (Hikami and Shiraishi, 1988; Cosentino et al., 2003; Zhan et al., 2008), RWIVs of stay cable occur when the inclination angle is in the range between 25° and 45°. Therefore the relevant calculation parameter was chosen to take the values 15°, 20°, 25°, 30°, 35°, 40°, 45° and 50° at an indicative wind yaw angle of 22°. As the formation and oscillation of the upper rivulet should be the main factor of RWIVs (Verwiebe and Ruscheweyh, 1998; Peil and Nahrath, 2003; Gu and Du, 2005), the lower rivulet features and dynamic behaviour are considered out of scope for this study. Fig.9 shows the influence of the inclination angle on the relative across-wind cable displacement amplitude and the upper rivulet thickness. It can be seen that the stay cable vibrates stronger at the inclination angles of 15° and 50°. With the increase of inclination angle, the relative cable amplitude gradually decreases at first and then increases to the maximum amplitude of about 0.59 at the inclination angle of 50°. The minimum relative cable amplitude 0.02 occurs at the inclination

angle of 40°. However, the upper rivulet thickness changes very slightly with the increase of inclination angle. These results indicate that the upper rivulet thickness appears to have a nonlinear complex (and not one-to-one) relationship with the cable vibration amplitude.

Fig.10 shows the influence of inclination angle on the upper rivulet position (i.e. of the centroid) and its oscillation range. The oscillation range is considered to be the angle between the extremes of the upper rivulet positions. With the increase of inclination angle, the upper rivulet kept moving at the windward side in a clockwise direction (see Fig.2). While the upper rivulet oscillation range became smaller at first it then became larger, which is the same trend as the cable vibration amplitude. Therefore, the oscillation range of the upper rivulet has a direct correlation with cable vibration, where to some extent a larger oscillation range for the upper rivulet may cause a larger cable vibration.

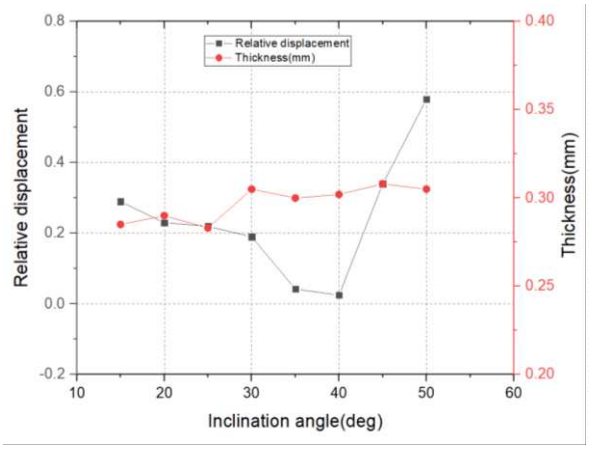

Fig.9 Influence of inclination angle on cable vibration amplitude and upper rivulet thickness

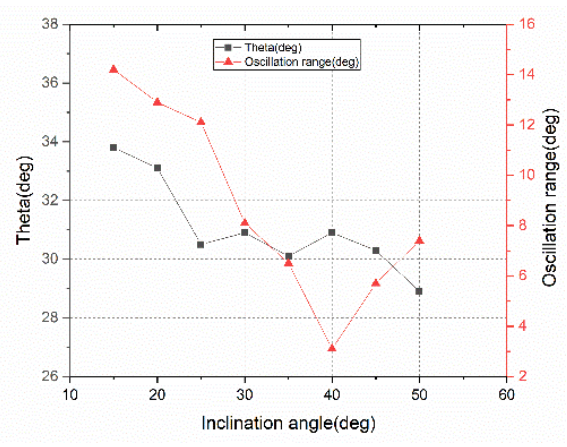

Fig.10 Influence of inclination angle on upper rivulet position and oscillation range

Fig.11 shows the influence of inclination angle on the aerodynamic coefficients. With the increase of inclination angle, the mean lift coefficient of the cable remained relatively stable at 0.26, while the aerodynamic drag coefficient slightly increased from 1.72 to 1.91. Fig.12 shows the influence of inclination angle on the dynamics of the aerodynamic coefficients. The variation trend is similar to the variation of cable vibration displacement. Thus, there is clear causal connection of both the unsteady lift and drag aerodynamic forces to the observed cable vibration amplitudes; still with some insensitivity for their mean values.

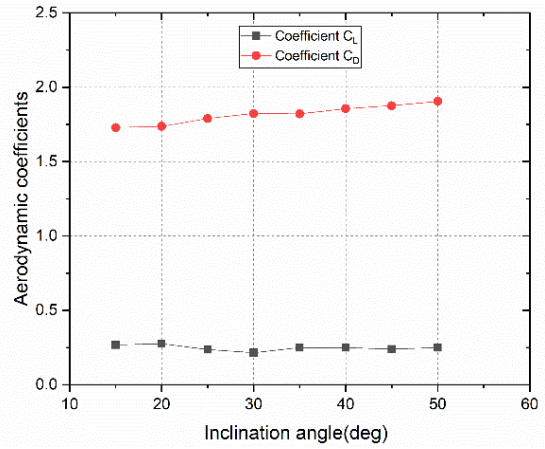

Fig.11 Influence of inclination angle on aerodynamic coefficients

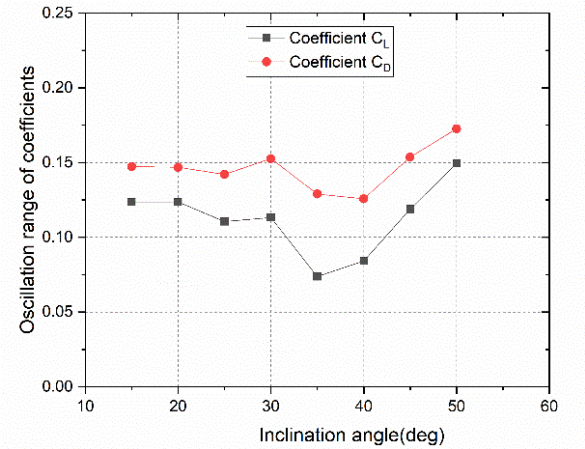

Fig.12 Influence of inclination angle on oscillation range of aerodynamic coefficients

Fig.13 and Fig.14 show the influence of inclination angle on cable vibration, upper rivulet oscillation frequency and amplitude. The dominant frequency of cable vibration and upper rivulet oscillation kept stable at 1.485Hz, which is approximately the natural frequency of the cable. However, the amplitude of both decreases until $\alpha = 40°$ and then increases to the maximum value, which is the same trend as that for the cable vibration displacement. Interestingly, with the increase of cable inclination angle the vortex phenomenon appears strongly for the inclination range from $\alpha = 35°$ to $\alpha = 50°$; the energy/variance of aerodynamic lift at the vortex frequency is much larger than that at the cable vibration frequency (coincident with the upper rivulet oscillation frequency). Thus, the increase of cable vibration amplitude beyond $\alpha = 40°$, could be connected to the appearance of enhanced vortex oscillations in the lift force; here the combination of self-excited RWIVs and vortex vibrations, which could further exacerbate the cable stressing were not considered explicitly but would be of great interest for a follow-up study.

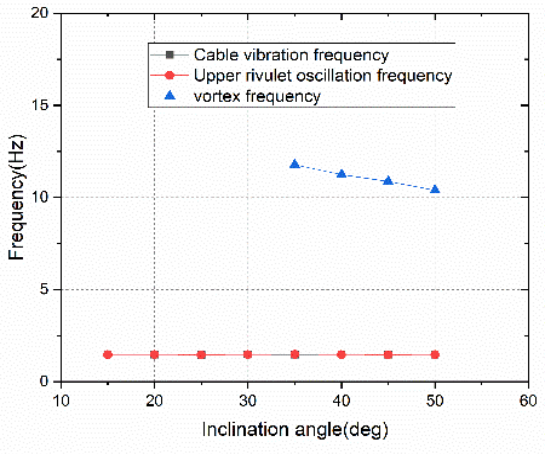

Fig.13 Influence of inclination angle on cable vibration and upper rivulet oscillation frequency

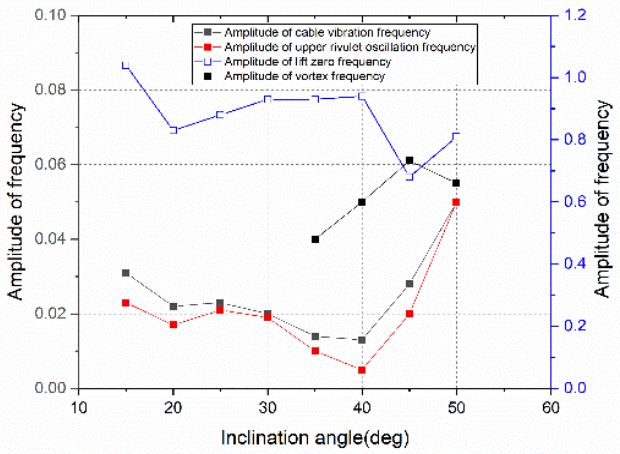

Fig.14 Influence of inclination angle on cable vibration and upper rivulet oscillation frequency amplitude

4.3 Effect of wind yaw angle

Again based on previous wind tunnel tests (Cosentino et al., 2003; Zhan et al., 2008), RWIVs of stay cables occur when the wind yaw angle β is at the range of $20°$ and $50°$. Therefore, the wind yaw angle from $15°$ to $55°$ at an indicative constant inclination angle, $30°$, was analysed in this part. Fig. 15 shows the influence of wind yaw angle on relative cable vibration amplitude and upper rivulet thickness. It can be seen that the relative cable amplitude keeps almost idle for the wide wind yaw angle range of $15°$ to $55°$; the mean relative cable vibration amplitude is 0.17. While the thickness of upper rivulet increases rapidly at first it then keeps stable from the wind yaw angle of $35°$ onwards. The maximum and minimum upper rivulet thickness are 0.73mm and 0.04mm respectively. The influence of wind yaw angle on upper rivulet position and oscillation range is displayed in Fig.16. The position of the upper rivulet around the cable keeps stable at $\theta = 34.6°$ and the oscillation range of it experiences limited changes, which is similar to the cable vibration displacement.

Fig.17 shows the influence of wind yaw angle on the aerodynamic coefficients. The mean aerodynamic lift coefficient remains relatively stable at 0.85, while the mean aerodynamic drag coefficient drops from the extreme of 6.76 to 3.50. For the influence of wind yaw angle on aerodynamic coefficients variation range (or else their dynamics) shown in Fig. 18, the

variation trend is similar to that of the cable vibration displacement. This is not the same trend as that encountered for the inclination angle (i.e. see relatively stable drag) but it would be quite interesting to compare these.

Fig.19 and Fig.20 display the influence of wind yaw angle on cable and upper rivulet vibrations' frequency and amplitude. The dominant frequency for the cable and the upper rivulet fall close to the initial natural frequency of the cable; the energy/variance around this dominant frequency, like the cable vibration response, only changes slightly keeping a value which is quite low. Interestingly, at the wind yaw angle of 15° to 35°, there exists signs of some ordinary vortex phenomenon, but the energy around the nominal vortex frequency for the lift coefficient is not considerable, reaching a maximum of only 0.048 at $\beta = 15°$.

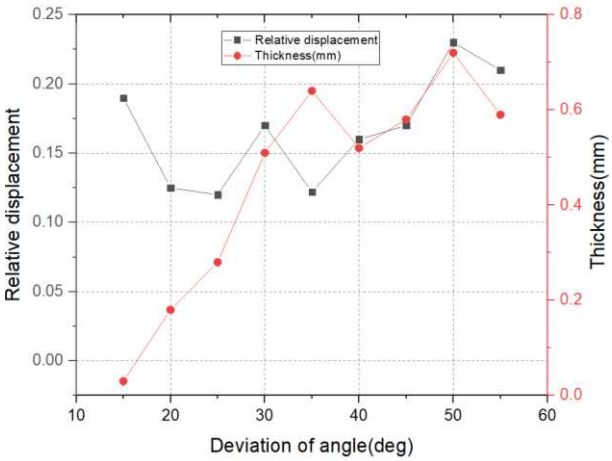

Fig.15 Influence of wind yaw angle on cable vibration amplitude and upper rivulet thickness

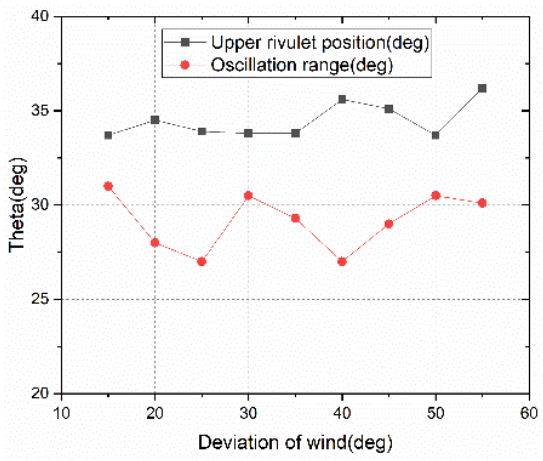

Fig.16 Influence of wind yaw angle on upper rivulet position and oscillation range

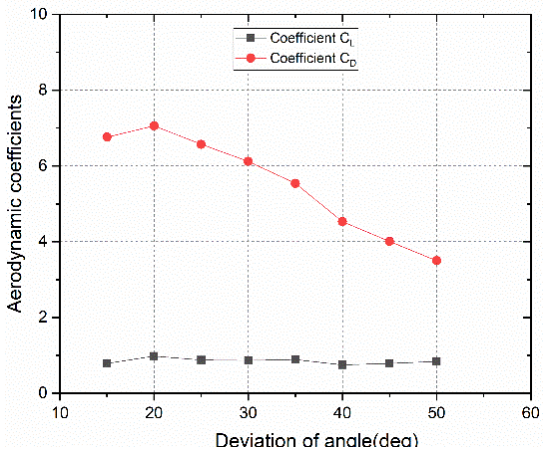

Fig.17 Influence of wind yaw angle on aerodynamic coefficients

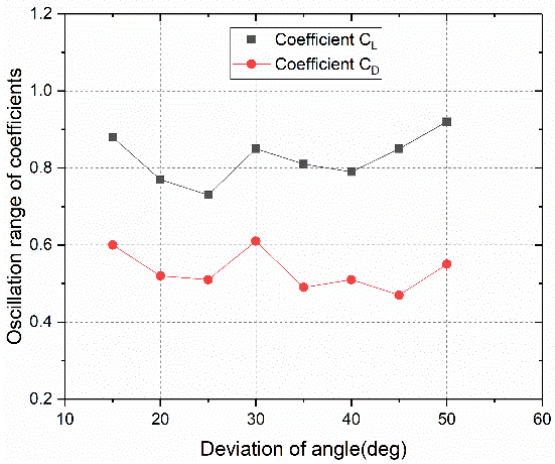

Fig.18 Influence of wind yaw angle on aerodynamic coefficients variation range

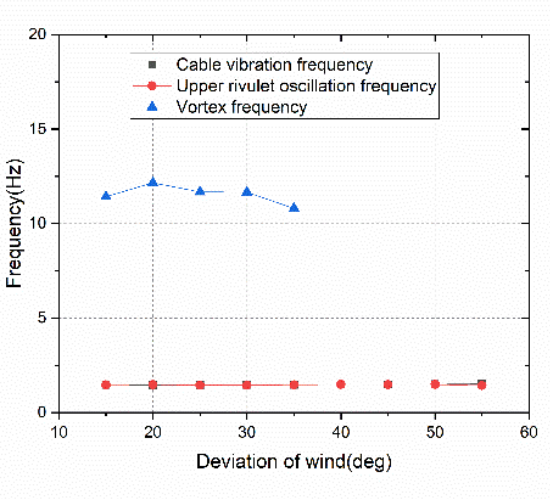

Fig.19 Influence of wind yaw angle on cable vibration and upper rivulet oscillation frequency

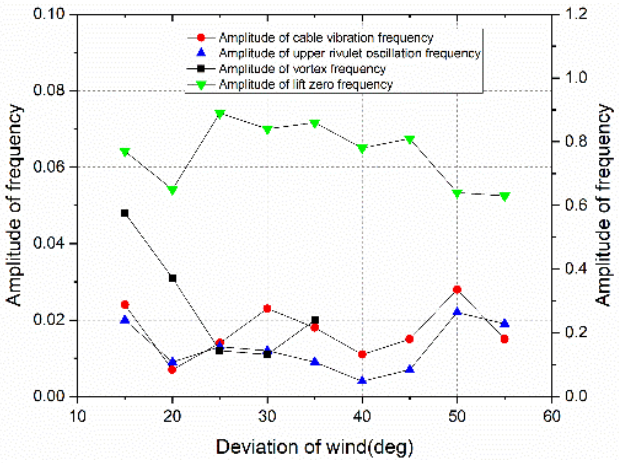

Fig.20 Influence of wind yaw angle on cable vibration and upper rivulet oscillation frequency amplitude

4.4 Effect of the height of rib

To investigate the influence of the rib height, heights of 1mm, 2mm, 3mm, 4mm, 5mm and no ribs were chosen as the calculation scenarios in this part. Fig.21 shows the influence rib height has on the relative cable vibration amplitude and the upper rivulet thickness. When the rib height increases the relative cable vibration displacement decreases gradually, though noting that the relative cable vibration displacement at 1mm ribs is larger than that of the bare circular cable. So low longitudinal ribs, not only seem unable to prevent the upper rivulet formation and motion but further enhance RWIVs. The thickness for the upper rivulet changed slightly with the maximum value 0.38mm and the minimum value 0.29mm not found at the points of extreme responses. Fig.22 shows the influence of rib height on upper rivulet position and oscillation range with a stronger influence on the latter.

Fig.23 and Fig.24 show the influence of rib height on the mean aerodynamic coefficients and their variation range. It can be seen that the oscillation range of the coefficients have a closer connection to the cable vibration displacement. Fig.25 and Fig.26 show the influence of rib height on the cable and upper rivulet oscillation frequency and amplitude. The dominant frequencies for both are close to the initial structural frequency of the stay cable. However, their variation trend is not identical showing at all cases non-monotonic behaviour and different inflection points..

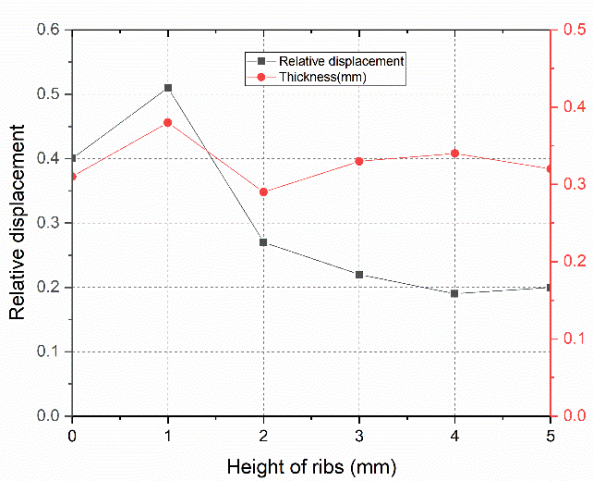

Fig.21 Influence of height of ribs on cable vibration amplitude and upper rivulet thickness

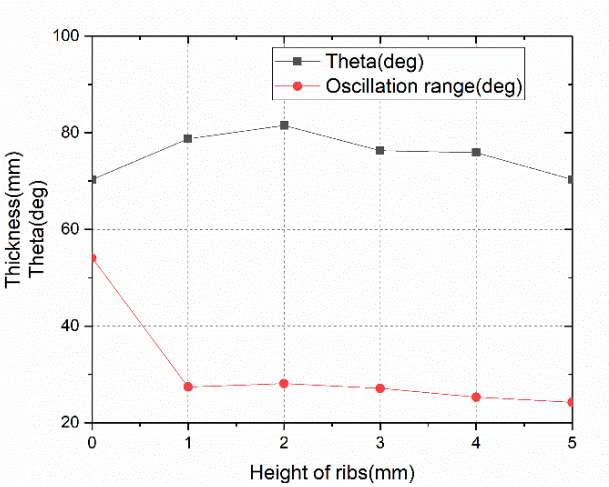

Fig.22 Influence of height of ribs on upper rivulet position and oscillation range

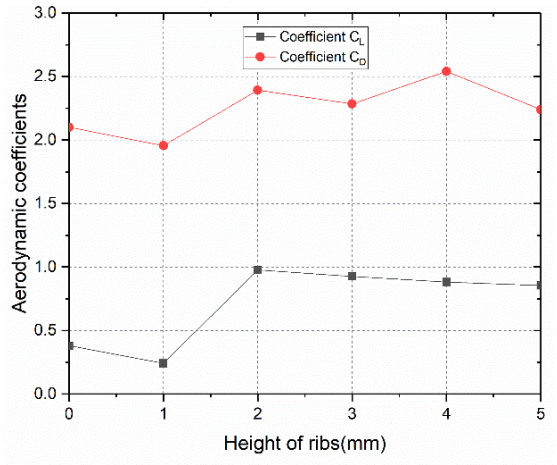

Fig.23 Influence of height of ribs on aerodynamic coefficients

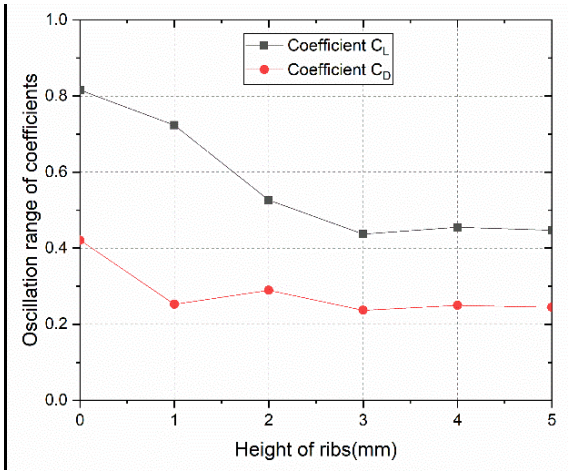

Fig.24 Influence of height of ribs on aerodynamic coefficients variation range

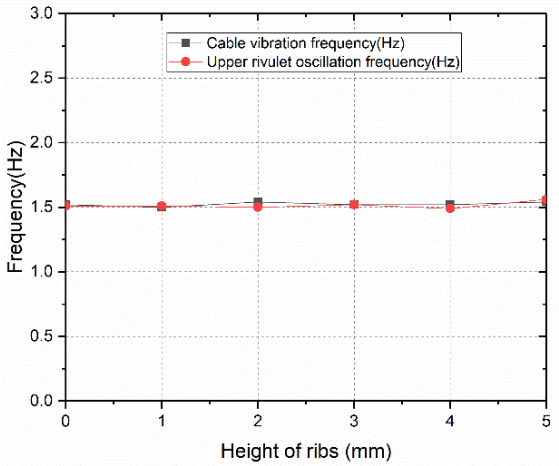

Fig.25 Influence of height of ribs on cable vibration and upper rivulet oscillation frequency

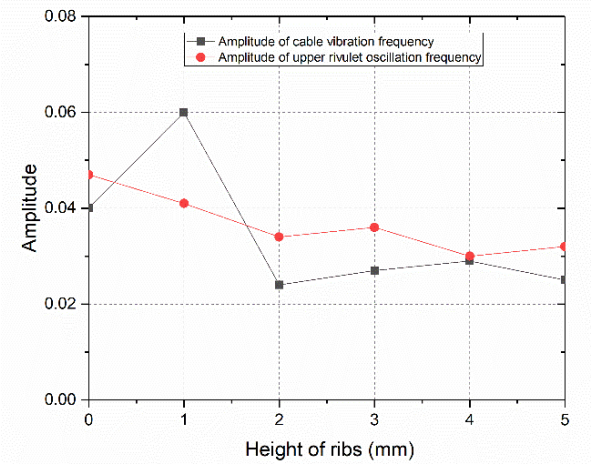

Fig.26 Influence of height of ribs on cable vibration and upper rivulet oscillation frequency amplitude

5. Conclusion

A new coupled theoretical model which could be used to analyse a stay cable with an arbitrary 2D shape (ideal for aerodynamic countermeasures) was established. For this model and for unimodal across-wind vibration response a number of approximations (e.g. no axial flow effect, single wind velocity, constant wind and air densities) were implemented for indicatively presenting the interaction of aerodynamic countermeasures to RWIVs. A stay cable with longitudinal ribs became the testbed for a series of numerical tests. Within them, the main factors that affect the rib-equipped cable RWIVs (inclination angle, wind yaw angle, the number and height of ribs) were considered. The effects of the longitudinal ribs on the cable vibration response, water film evolution and aerodynamic forces were analysed to investigate the inherent vibration mitigation mechanisms. The key conclusions from this work are:

(1) The most unfavourable conditions for all the quoted cable-rib parameters were independently (i.e. no coupling study) identified. For a wind yaw angle of $15°$, the maximum cable vibration response occurs at the inclination angle of $15°$ and $50°$. On the other hand, for an inclination of $30°$ the most unfavourable conditions occurred when the wind yaw angle approached $50°$ (still with a relative insensitivity to wind yaw angle). A suitable height and number of ribs should be considered, otherwise rib countermeasures may even amplify cable vibration displacements.

(2) For the cable with longitudinal ribs, the upper rivulet still exists, but its position and oscillation range is majorly affected. The oscillation range of the upper rivulet seems to have a causal relationship to the cable vibration response. The existence of many longitudinal ribs could have a detuning effect on the upper rivulet motion; this seems reminiscent of the vortex shedding inhibiting for circular cylinders in the critical Reynolds number range.

(3) For the inclination angle of $35°\sim50°$ and wind yaw angle of $15°\sim35°$, RWIVs self-excited force components and ordinary vortex shedding components co-exist within lift signals. Interestingly, the energy associated with vortex shedding seems considerable and is expected to lead into hybrid phenomena while contributing to the amplification or mitigation of observed vibrations.

Acknowledgements

The authors gratefully appreciate the support of China Scholarship Council.

References

Ahmad, J., Cheng, S., Ghrib, F., 2015. Effect of number of cross-tie lines on the in-plane stiffness and modal behaviour classification of orthogonal cable networks with multiple lines of transverse flexible cross-ties. *Journal of Engineering Mechanics ASCE* **142**(4) 04015106.

Bi, J.H., Wang, J., Shao, Q., 2013. 2D numerical analysis on evolution of water film and cable vibration response subject to wind and rain. Journal of Wind Engineering and Industrial Aerodynamics **121**, 49-59.

Bi, J.H., Qiao, H.Y., Nikitas, N., Guan, J., Wang, J., Lu, P., 2018. Numerical modelling for rain wind induced vibration of cables with longitudinal ribs. Journal of Wind Engineering and Industrial Aerodynamics **178**, 69-79.

Caracoglia, L., Jones, N.P., 2007. Passive hybrid technique for the vibration mitigation of systems of interconnected stays. Journal of Sound and Vibration **307**, 849–864.

Casciati, F., Ubertini, F., 2008. Nonlinear vibration of shallow cables with semi-active tuned mass damper. Nonlinear Dynamics **53**, 89-106.

Cosentino, N., Flamand, O., Ceccoli, C., 2003. Rain–wind induced vibration of inclined stay cables, Part I: experimental investigation and physical explanation. Wind & Structures **6**, 471–484.

Fournier, J., Cheng, S., 2014. Impact of damper stiffness and damper support stiffness on the efficiency of a linear viscous damper in controlling stay cable vibrations. Journal of Bridge Engineering ASCE **19**(4) 04013022.

Gimsing, N.J., Georgakis, C.Y., 2012. Cable Supported Bridges - Concept and Design, Third Edition. John Wiley & Sons.

Gu, M., Du, X.Q., 2005. Experimental investigation of rain wind induced vibration of cables in cable-stayed bridges and its mitigation. Journal of Wind Engineering and Industrial Aerodynamics **93**, 79-95.

Gao, D.L., Chen, W.L., Eloy, C., Li, H. 2018. Multi-mode responses, rivulet dynamics, flow structures and mechanism of rain-wind induced vibrations of a flexible cable. Journal of Fluids and Structures 82: 154-172.

Gao, D.L., Chen, W.L., Zhang, R., Huang, Y. W., Li, H. 2019. Multi-modal vortex- and rain–wind-induced vibrations of an inclined flexible cable. Mechanical Systems and Signal Processing 118: 245-258.

Hikami, Y., Shiraishi, N., 1988. Rain-wind-induced vibrations of cables in cable stayed bridges. Journal of Wind Engineering and Industrial Aerodynamics 29, 409-418.

Hu, S. J., Zhou, S. H., 2001. Wind tunnel experiment research on rain wind induced vibration and its mitigation. Proceedings of the fifth wind engineering and technical aerodynamics, 2001, 264-270. (in chinese)

Hung, V.D., Katsuchi, H., Sakaki, I., Okado, E., Ariji, R., Yamada, H., 2016. Aerodynamic performance of spiral-rib cable under rain and dry conditions. Journal of Structural Engineering JSCE, 2016, 62A, 431-441.

Kleissl, K., Georgakis, C.T., 2011. Aerodynamic control of bridge cables through shape modification: A preliminary study. *Journal of Fluids and Structures* **27**, 1006-1020.

Katsuchi H, Yamada H, Sakaki I, Okado, E., 2017. Wind-Tunnel Investigation of the Aerodynamic Performance of Surface-Modification Cables. Engineering **3**(6), 817-822.

Li, W.B., Lin, Z.X., 2005. A study on aerodynamic control countermeasures to rain-wind induced vibration of cables in cable-stayed bridge. China Civil Engineering Journal **38**(5), 48-53. (in chinese).

Li, H., Chen, W.L., Xu, F., Li, F.C., 2010a. A numerical and experimental hybrid approach for the investigation of aerodynamic forces on stay cables suffering from rain wind induced vibration. *Journal of Fluid and Structures* **26**(7-8), 1195-1215.

Li, F.C., Chen, W.L., Li, H., Zhang, R., 2010b. An ultrasonic transmission thickness measurement system for study of water rivulets characteristics of stay cables suffering from wind–rain-induced vibration. Sensors and Actuators A: Physical **159**, 12–23.

Li, Y., Jing, H., Xia, Y., Xu, Y., Xiang, H., 2015. Measurement of rivulet movement on inclined cables during rain–wind induced vibration. Sensors and Actuators A: Physical **230**, 17-24.

Liu, Q.K., Zheng, Y.F., Zhao, S.B., Ma, W.Y., Liu, X.B., Chen, J.J., 2016. Experimental study on helical line parameters and rain-wind induced vibration control of stay cables. Engineering Mechanics. 33 (10), 138–144.

Lemaitre, C., Alam, M.M., Hémon, P., Langre, E., Zhou, Y., 2006. Rainwater rivulets on a cable subject to wind. Comptes Rendus Mécanique **334**, 158-163.

Lemaitre, C., Hémon, P., Langre, E., 2007. Thin water film around a cable subject to Wind. Journal of Wind Engineering and Industrial Aerodynamics **95**(9), 1259-1271.

Matsumoto, M., Shirato, H., Yagi, T., Goto, M., Sakai, S., Ohya, J., 2003. Field observation of the full-scale wind-induced cable vibration. Journal of Wind Engineering and Industrial Aerodynamics **91**, 13-26.

Sun L, Hong D, Chen L. Cables interconnected with tuned inerter damper for vibration mitigation [J]. *Engineering Structures*, 2017, 151:57-67.

Verwiebe, C., Ruscheweyh, H., 1998. Recent research results concerning the exciting mechanisms of rain-wind-induced vibrations. *Journal of Wind Engineering and Industrial Aerodynamics* **74-76**(98), 1005-1013.

Peil, U., Nahrath, N., 2003. Modelling of rain-wind induced vibration. Wind & Structures **6**(1), 41-52.

Zhan, S., Xu, Y.L., Zhou, H.J., Shum, K.M. 2008. Experimental study of wind–rain induced cable vibration. Journal of Wind Engineering and Industrial Aerodynamics **96**, 2438-2451.